Chemical Science

ROYAL SOCIETY OF CHEMISTRY

EDGE ARTICLE

View Article Online
View Journal | View Issue

Cite this: *Chem. Sci.*, 2020, **11**, 10255

All publication charges for this article have been paid for by the Royal Society of Chemistry

Received 14th July 2020
Accepted 8th September 2020

DOI: 10.1039/d0sc03846f

rsc.li/chemical-science

Chemically driven superstructural ordering leading to giant unit cells in unconventional clathrates $Cs_8Zn_{18}Sb_{28}$ and $Cs_8Cd_{18}Sb_{28}$†

Bryan Owens-Baird,[ab] Philip Yox,[abc] Shannon Lee,[ab] Xian B. Carroll,[d] Suyin Grass Wang,[e] Yu-Sheng Chen,[e] Oleg I. Lebedev[c] and Kirill Kovnir*[ab]

The unconventional clathrates, $Cs_8Zn_{18}Sb_{28}$ and $Cs_8Cd_{18}Sb_{28}$, were synthesized and reinvestigated. These clathrates exhibit unique and extensive superstructural ordering of the clathrate-I structure that was not initially reported. $Cs_8Cd_{18}Sb_{28}$ orders in the $Ia\bar{3}d$ space group (no. 230) with 8 times larger volume of the unit cell in which most framework atoms segregate into distinct Cd and Sb sites. The structure of $Cs_8Zn_{18}Sb_{28}$ is much more complicated, with an 18-fold increase of unit cell volume accompanied by significant reduction of symmetry down to $P2$ (no. 3) monoclinic space group. This structure was revealed by a combination of synchrotron X-ray diffraction and electron microscopy techniques. A full solid solution, $Cs_8Zn_{18-x}Cd_xSb_{28}$, was also synthesized and characterized. These compounds follow Vegard's law in regard to their primitive unit cell sizes and melting points. Variable temperature *in situ* synchrotron powder X-ray diffraction was used to study the formation and melting of $Cs_8Zn_{18}Sb_{28}$. Due to the heavy elements comprising clathrate framework and the complex structural ordering, the synthesized clathrates exhibit ultralow thermal conductivities, all under 0.8 W m^{-1} K^{-1} at room temperature. $Cs_8Zn_9Cd_9Sb_{28}$ and $Cs_8Zn_{4.5}Cd_{13.5}Sb_{28}$ both have total thermal conductivities of 0.49 W m^{-1} K^{-1} at room temperature, among the lowest reported for any clathrate. $Cs_8Zn_{18}Sb_{28}$ has typical p-type semiconducting charge transport properties, while the remaining clathrates show unusual n–p transitions or sharp increases of thermopower at low temperatures. Estimations of the bandgaps as activation energy for resistivity dependences show an anomalous widening and then shrinking of the bandgap with increasing Cd-content.

Introduction

Intermetallic clathrates are a diverse class of caged materials that span much of the periodic table and are considered to be promising materials in a number of high-impact fields, such as: photovoltaics, thermoelectric materials, superconductors, Li-ion batteries, and gas-storage materials.[1,2] Within the group of intermetallic clathrates, there is a further subdivision: conventional and unconventional clathrates. Conventional clathrates have a majority of their framework elements composed of group 14 tetrel elements (Si, Ge, or Sn); with the majority of known intermetallic clathrates falling under this classification, including the well-studied $Ba_8Ga_{16}Ge_{30}$ clathrate.[1,3] Unconventional clathrates, or tetrel-free clathrates, are typically formed by the combination of late- or post-transition metals (Cu, Ni, Zn, Cd, Au, *etc.*) and group 15 pnictogen elements (P, As, or Sb), such as $Ba_8Cu_{16}P_{30}$, $EuNi_2P_4$, or $SrNi_2P_4$.[4–8]

For unconventional clathrates, superstructural ordering of the framework and guest positions is common. For example, $Ba_8M_{16}P_{30}$ (M = Cu, Au) clathrates exhibit superstructural order of their framework, in which M and P segregate into distinct sites.[5,9] This ordering has been rationalized as the minimization of M–M interactions within the framework and the preferential formation of M–P or P–P bonds. Superstructural ordering in these systems is sensitive to inclusion of an additional elemental component. Modification of the $Ba_8Cu_{16}P_{30}$ clathrate with Ge or Zn forms the $Ba_8Cu_{14}Ge_6P_{26}$ and $Ba_8Cu_{16-x}Zn_{x+y}P_{30-y}$ clathrate systems, and shows a collapse of the superstructure into the archetype cubic subcell.[10,11]

[a]*Department of Chemistry, Iowa State University, Ames, IA 50011, USA. E-mail: kovnir@iastate.edu*

[b]*Ames Laboratory, U.S. Department of Energy, Ames, IA 50011, USA*

[c]*Laboratorie CRISMAT, UMR 6508, CNRS-ENICAEN, Caen 14050, France*

[d]*Department of Chemistry, University of Tennessee, Knoxville, TN 37996, USA*

[e]*NSF's ChemMatCARS, Center for Advanced Radiation Source, The University of Chicago, Argonne, USA*

† Electronic supplementary information (ESI) available: Experimental details, figures, and tables pertinent to characterization techniques used: powder and single crystal X-ray diffraction, electron microscopy, energy dispersive X-ray spectroscopy, differential scanning calorimetry, spark plasma sintering, and transport property measurements. CCDC 2015862–2015864. For ESI and crystallographic data in CIF or other electronic format see DOI: 10.1039/d0sc03846f

Recently, the first transition-metal free unconventional clathrate, $Cs_8In_{27}Sb_{19}$, was discovered and shown to retain the high hole mobility found in its binary counterpart: InSb.[12] Many other binary metal antimonides also display highly attractive properties, such as the Zn–Sb binaries for thermoelectric applications.[13–17] We hypothesized that clathrates based on {Zn,Cd}-Sb frameworks may inherit transport properties of corresponding binary antimonides. The unconventional clathrates $Cs_8M_{18}Sb_{28}$ (M = Zn, Cd) were originally reported in 2009 to crystallize in the archetypical type-I clathrate structure in the cubic space group $Pm\bar{3}n$ (no. 223).[18] In such a structure, at least one framework site is mixed occupied by metal and antimony and statistically, M–M bond are allowed. This is in drastic difference to $Cs_8In_{27}Sb_{19}$ clathrate which exhibits a full ordering of In and Sb over different framework sites in the ordered superstructure of clathrate-I.[12] The M/Sb ordering is important because electronic band structure calculations showed $Cs_8Zn_{18}Sb_{28}$ and $Cs_8Cd_{18}Sb_{28}$ to be either small bandgap semiconductors or metals depending on the chosen ordered model derived from disordered $Pm\bar{3}n$ structure.[19] While $Cs_8Zn_{18}Sb_{28}$ and $Cs_8Cd_{18}Sb_{28}$ have been reported, their physical properties were never explored, and the potential ordering of their complex crystal structures was not discussed.

In the current work, we explore the complexities of the two different and unique superstructural orderings for $Cs_8Zn_{18}Sb_{28}$ and $Cs_8Cd_{18}Sb_{28}$. Crystallographic structures are probed using synchrotron single-crystal (SC-XRD) and powder X-ray diffraction (PXRD), high-angle annular scanning transmission electron microscopy (HAADF-STEM), and electron diffraction (ED) techniques. Furthermore, the full range of solid-solutions for the clathrate system $Cs_8Zn_{18-x}Cd_xSb_{28}$ has been synthesized. These quaternary mixed-metal clathrates do not show any indication of superstructural ordering. Primitive unit cell sizes and thermal melting points follow Vegard's law. The formation and melting of $Cs_8Zn_{18}Sb_{28}$ is thoroughly studied using variable temperature *in situ* synchrotron PXRD. Thermal and charge transport properties were characterized for $Cs_8Zn_{18-x}Cd_xSb_{28}$ (x = 0, 4.5, 9, 13.5, 18), showing complex electronic behaviors at low temperatures.

Experimental details

Synthesis

Handling and manipulation of starting materials and products was carried out in an argon filled glovebox ($p(O_2)$ < 0.1 ppm). All chemicals were used as received: Cs metal (99.8%, Alfa Aesar), Zn granules (99.8%, Alfa Aesar), Cd shot (99.95%, Alfa Aesar), and Sb shot (99.999%, Alfa Aesar).

All clathrate samples were synthesized *via* reaction of the elements. Stoichiometric amounts of starting materials were loaded into Ta ampoules that were welded shut under argon atmosphere. The Ta ampoules were enclosed into silica ampoules, which were evacuated, and flame sealed. The ampoules were heated from room temperature to 823 K over 10 h, annealed for 120 h, and cooled to room temperature naturally in the turned-off furnace. Samples were ground and reannealed under the same conditions two additional times to ensure homogeneity, producing light-gray powder. Single-phase samples were collected for each composition as products of third annealing.

Synthesis of $Cs_8Zn_{18}Sb_{28}$ can also be achieved using a CsCl method.[18,20] Mg, Zn, Sb, and CsCl in a 8 : 18 : 28 : 160 ratio, were loaded into an alumina crucible and sealed within an evacuated silica jacket. The ampoule was heated from room temperature to 948 K over 17 h, annealed for 120 h, and cooled to room temperature naturally. The samples were then washed in H_2O for 1 hour to dissolve CsCl and $MgCl_2$ salts. The annealing time was further explored by varying the annealing times of the samples at 1, 2, 3, and 5 days. These results showed the formation of clathrate phase at 2 days annealing but did not begin to predominately form until 3 days of reaction time.

Characterization

The synthesized samples were characterized by single-crystal X-ray diffraction (SC-XRD), powder X-ray diffraction (PXRD), *in situ* variable temperature synchrotron powder X-ray diffraction, high-resolution synchrotron powder X-ray diffraction, synchrotron single-crystal X-ray diffraction, differential scanning calorimetry (DSC), scanning electron microscopy (SEM), electron diffraction (ED), high-angle annular dark field scanning transmission electron microscopy (HAADF-STEM), energy dispersive X-ray spectroscopy (EDX), and with a Quantum Design Physical Property Measurement System. Additional information can be found in the ESI.†

Results and discussion

Superstructural ordering of $Cs_8Cd_{18}Sb_{28}$

$Cs_8M_{18}Sb_{28}$ (M = Zn, Cd) were reported to crystallize in the archetypical type-I clathrate crystal structure in the $Pm\bar{3}n$ space group with a ~12 Å.[18] Reinvestigation into the $Cs_8M_{18}Sb_{28}$ systems began with the discovery of many additional reflections in the single crystal diffraction patterns. Electron diffraction confirms these extra reflections represent a superstructural ordering in $Cs_8M_{18}Sb_{28}$.

In-house single-crystal XRD studies of $Cs_8Cd_{18}Sb_{28}$ led to a structure solution in the body-centered $Ia\bar{3}d$ space group (no. 230; Z = 8) with a unit cell length of a = 24.3160(5) Å. This ordered cell is eight times larger than the archetypical type-I clathrate structure initially reported for $Cs_8Cd_{18}Sb_{28}$ (Fig. 1).[18] The $Pm\bar{3}n$ subcell structure has five positions: the 2a and 6d, which are guest atom positions; and 6c, 16i, and 24k, which are framework positions. An assignment of elements on the subcell framework positions was generalized to both Cd and Sb, whereas the initial report[18] indicated that only the 24k position was jointly occupied by Cd and Sb. The supercell for $Cs_8Cd_{18}Sb_{28}$ can be solved in a variety of cubic space groups, such as $Ia\bar{3}d$ (no. 230), $Ia\bar{3}$ (no. 206), and $I2_13$ (no. 199), while exact determination of Cd and Sb distribution over framework sites is challenging due to similarity of their scattering factors. To help resolve this issue, single crystal X-ray diffraction data was collected at a synchrotron while utilizing ultra-low temperatures (10 K) to minimize thermal motion. The high-

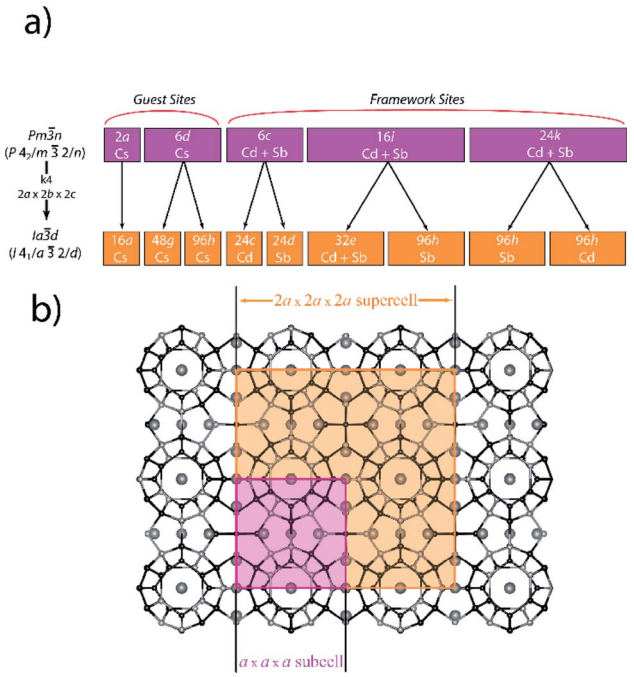

Fig. 1 (a) Diagram showing the group–subgroup Wyckoff site splitting from the ideal type-I clathrate $Pm\bar{3}n$ subcell into the $Ia\bar{3}d$ supercell for $Cs_8Cd_{18}Sb_{28}$. Note, that in the $Pm\bar{3}n$ subcell all framework sites were assigned as mixed Cd/Sb based on our solution in the subcell. The reported solution in ref. 18 has different occupancies which we were not able to reproduce. (b) Projection of the clathrate superstructure with the subcell and supercell emphasized in purple and orange, respectively.

resolution synchrotron data was used for the final refinement, providing a high sin θ/λ of 1.19 $Å^{-1}$ and data/parameters ratio of 133. Assignment of Cd and Sb sites was systematically performed by allowing each framework site occupancy to independently refine. For an incorrectly assigned position, the occupancy would raise or lower toward the correct electron count. For instance, a Sb site whose variable occupancy refined to 0.93(1)–0.96(1) may indicate that the position is Cd, while a refinement that was close to unity within one e.s.d. would suggest Sb to be the correct assignment. This process was repeated for all framework sites multiple times until a stable model was achieved.

As the unit cell transforms to the $Ia\bar{3}d$ superstructure, the five subcells positions split into eight sites; two guest (16a and 48g) and six framework sites (24c, 24d, 32e, and three 96h) (Fig. 1a). Within this model, every framework atomic site, with the exception of 32e, is solely occupied by one type of element, either Cd or Sb, indicating a possible driving force behind the superstructural ordering. The 32e site splits into three partially occupied positions within close proximity (<0.5 Å) to each other. Additionally, the 48g position, which corresponds to the Cs guest position in the large tetrakaidecahedron cage, is found to shift from the cage center to a 96h position that is off centered with respect to tetrakaidecahedron cage. It was initially believed that the split positions could be resolved by lowering the space group symmetry, to break this 32e site into multiple sites that could then be refined as Cd and Sb separately. Reduction to $Ia\bar{3}$ results in the splitting of the 32e site to two 16c positions; while in the $I2_13$ space group the 32e site splits into four 8a sites. Subsequent structure refinements within these space groups did not alleviate the mixed occupancy problem. For the lower symmetry solutions, every site generated from 32e site is still found to split into two sites with similar Cd/Sb occupancies and the corresponding *R*-values did not decrease below the *R*-values found in the initial $Ia\bar{3}d$ model. For that reason, we are presenting the higher symmetry $Ia\bar{3}d$ model as the superstructure for $Cs_8Cd_{18}Sb_{28}$ (Tables S1–S3†).

The 32e site proved to be quite challenging to refine. It splits into three individual positions, assigned as Sb(61), Sb(62), and Cd(63). The Sb(62) site refines to a position that is a short distance to the Cs(1) site (3.38 Å) which is substantially closer than the other Cs-framework distances. A small concentration of vacancies of Cs(1) was detected (~2%) which correlates to the refined occupancy of Sb(62), for this reason the occupancy of Cs(1) and Sb(62) were constrained as mutually exclusive in the final refinement. Assigning the spilt 32e site as either Cd or Sb resulted in correlated refinement, where the amount of Cd was either slightly higher or lower than 75%. Close proximity of the sites, similar scattering factors of Cd and Sb, and the correlations of site occupancy factors and atomic displacement parameters (ADPs) (despite ADPs were constrained to be equal for all three sites) were challenging to refine, even for the high-quality 10 K dataset. In the final refinement, Cd(63) was constrained to be 75% occupied, while two other sites were set to be Sb and allowed to refine, resulting in a nearly stoichiometric $Cs_{7.95}Cd_{18}Sb_{27.99}$ composition. In such a refinement, the Sb(62) occupancy appeared to be identical to Cs(1) vacancies within one e.s.d. Mentioned above, the Cs(2) position that resides within the large tetrakaidecahedron cage, is split into two positions. The main Cs(2) position is 79% occupied, while the secondary off-center Cs(22) site is 21% occupied. Previous low temperature clathrate studies in $Ae_8Ga_{16}Ge_{30}$ (Ae = Sr, Ba, Eu) have showed that the guest position in the larger tetrakaidecahedron cage can split into many partially occupied positions around the cage.[21–25] The refined Cd and Sb framework sites arrange in such a way that the number of Cd–Cd bonds are minimized, agreeing well with previous reports of superstructural ordering in unconventional clathrates.[9,10,12] The split 32e position is the exception to this notion, as it forms a Cd(63)–Cd(63) interaction in 50% of the cases.

Recently reported by us $Cs_8In_{27}Sb_{19}$ clathrate also shows a 2×2×2 superstructure in the $Ia\bar{3}$ space group, with a full ordering of In and Sb atoms over different framework sites.[12] The driving force for this ordering was suggested to be maximization of In–Sb interactions while minimizing In–In and Sb–Sb contacts. In the case of $Cs_8Cd_{18}Sb_{28}$, a slightly different and complex ordering is observed including one site, with mixed occupancies of Cd and Sb. We hypothesize that this complexity is driven by the detected vacancies and displacement in Cs guest positions. We will demonstrate later that higher concentration of Cs vacancies leads to a much more complex ordering in the case of $Cs_8Zn_{18}Sb_{28}$.

To get a better understanding of the superstructural ordering, high-angle annular dark-field scanning transmission electron microscopy (HAADF-STEM) and electron diffraction (ED) were utilized. ED confirms a superstructural ordering of $Cs_8Cd_{18}Sb_{28}$, due to the presence of diffraction spots which cannot be indexed in the $Pm\bar{3}n$ subcell with $a = 12.16$ Å unit cell parameter (Fig. 2). To fit these observed reflections, a doubling of the a-parameter is required, supporting the presence of a $2\times2\times2$ superstructure. Unexpectedly, ED studies revealed a presence of additional high intensity diffraction peaks, (110) and (200), which are expected to be either systematically absent (110) or have intensity close to zero (200) for our $Ia\bar{3}d$ superstructural model, note that intensities close to zero are expected for both reflections in $Ia\bar{3}$ and $I2_13$ models. We hypothesize that these intensities are due to double-diffraction which has been observed for other clathrate systems.[9,11] Long range ordering corresponding to (110) and (200) reflections was not observed by either synchrotron single crystal or high-resolution powder X-ray diffraction experiments (Fig. S7†), thus supporting a double-diffraction hypothesis. High-resolution HAADF-STEM images along main cubic zone axis (Fig. 3) show a good crystallinity of the material and demonstrates an agreement with $Ia\bar{3}d$ ($a = 24.32$ Å) superstructural model.

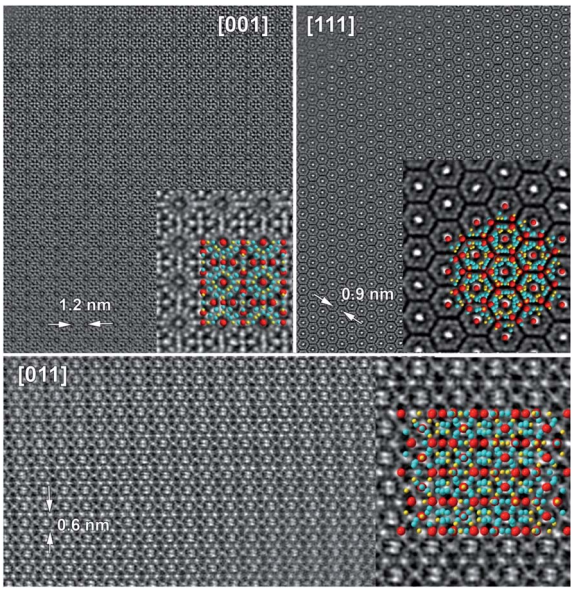

Fig. 3 HAADF-STEM images for $Cs_8Cd_{18}Sb_{28}$ along main zone axis: the [001] (top left), [111] (top right), and [011] (bottom) zone axis. Magnified images and overlaid structural models are given as insets, where Cs – red; Cd – yellow; and Sb – light blue.

Superstructural ordering of $Cs_8Zn_{18}Sb_{28}$

$Cs_8Zn_{18}Sb_{28}$ proved to be more difficult to structurally elucidate than $Cs_8Cd_{18}Sb_{28}$. Single-crystal XRD experiments showed a huge number of reflections, indicative of a large unit cell. High-resolution synchrotron powder diffraction confirmed the presence of multiple weak superstructural reflections. Single crystal indexing software suggested a large ~35 Å primitive cubic unit cell, which would be $3\times3\times3$ superstructure of the reported primitive unit cell of 11.70 Å. Unfortunately, the collected data, either conventional lab or synchrotron based, could not be solved. Numerous "single crystals" from many samples were collected and measured, all producing similar results.

ED and HAADF-STEM were utilized to elucidate the true structure of $Cs_8Zn_{18}Sb_{28}$ clathrate samples. Investigating what would be the ED $[001]_C$ zone for $Pm\bar{3}n$ primitive cubic structure with 11.70 Å, clearly shows the absence of expected 4-fold rotational symmetry (Fig. 4 middle bottom). There are additional spots along one $[110]_C$ diagonal direction, but not along the perpendicular direction, indicating possible orthorhombic ordering. Similarly, additional reflections are clearly observed in the ED pattern of what would be the $[111]_C$ zone in the primitive cubic structure (Fig. 4 top left). Based on these additional reflections and their location, the unit cell of $Cs_8Zn_{18}Sb_{28}$ may be an orthorhombic with one edge three times longer than the other one. ED studies also shed light on the failure of X-ray single crystal diffraction experiments. The selective area ED (SAED) patterns shown on Fig. S1† was obtained from multiple different small size areas selected with small apertures within one single crystallite. Instances of twinning can be seen by visually comparing the HAADF-STEM images and

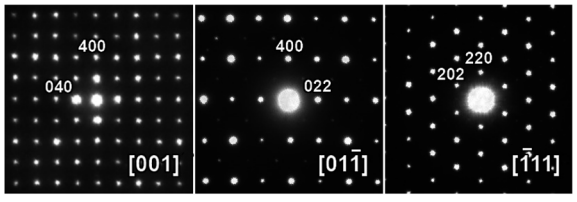

Fig. 2 ED patterns for $Cs_8Cd_{18}Sb_{28}$ along main zone axis ([001], [01$\bar{1}$], and [$\bar{1}$11]) indexed based on cubic $Ia\bar{3}d$ structure with $a = 24.32$ Å unit cell parameter.

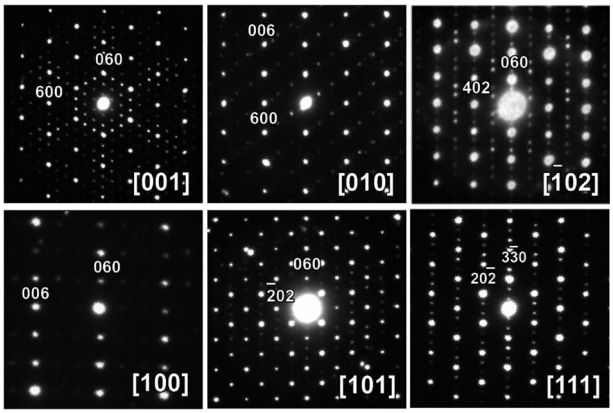

Fig. 4 ED patterns for select $Cs_8Zn_{18}Sb_{28}$ zone axis: [001], [100], [010], [101], [$\bar{1}$02], and [111]. All ED patterns indicate an absence of cubic symmetry and can be indexed using a monoclinic $P2$ structural model ($a = 29.86$ Å, $b = 51.76$ Å, $c = 21.12$ Å, $\alpha = \beta = \gamma = 90.0$). Note, the [101], [010], and [001] monoclinic directions correspond to the $[001]_C$, $[110]_C$, and $[111]_C$ directions of the primitive $Pm\bar{3}n$ clathrate cubic cell, respectively.

corresponding ED (Fig. S1†). Similar behavior has been previously reported for $Ba_8Au_{16}P_{30}$, in which ED showed both a large twinned unit cell and a smaller single-domain orthorhombic unit cell, with the size of the electron beam determining which pattern was observed.[9] This nano-twinning of the crystallites prevented the single crystal structural elucidation of both $Ba_8Au_{16}P_{30}$ and $Cs_8Zn_{18}Sb_{28}$.

HAADF-STEM images of $Cs_8Zn_{18}Sb_{28}$ crystallites shows the complexity of the crystal structure (Fig. 5). Considering only Cs atomic columns, the superstructure can be resolved in a trigonal $P\bar{3}c1$ (no. 165) $\sqrt{2}\times\sqrt{2}\times\sqrt{3}$ superstructure. Such superstructural ordering was observed for $Ba_8Cu_{12}Zn_5P_{29}$.[10] Additionally, the columns of framework atoms forming hexagons around columns of Cs atoms clearly violates the 3-fold rotation. The highlighted hexagons (Fig. 5 right) only allow for a single 2-fold rotation axis to be present within the structure. Based on these high-resolution images of the structure, the model symmetry was further lowered to $P2$ (no. 3) and unit cell dimensions increased to $\sqrt{6}\times3\sqrt{2}\times\sqrt{3}$ (Fig. 6). This low symmetry model fits reasonably well with the collected HAADF-STEM and ED data. High-resolution synchrotron powder X-ray diffraction also supports the presence of a complex superstructure (Fig. 7). Several superstructural peaks are detected, many of which are not produced by the higher symmetry primitive $Pm\bar{3}n$ subcell nor by the trigonal $P\bar{3}c1$ supercell.

In the resulting $P2$ superstructure there are 78 guest Cs sites and 420 framework sites. The exact distribution of Zn and Sb over 420 framework sites is difficult to determine solely based on electron diffraction and high-resolution electron microscopy data. The reported model is our best attempt to distribute the 324 Zn and 504 Sb atoms over 420 sites to minimize Zn–Zn interactions, similar to the cases of $Cs_8Cd_{18}Sb_{28}$, $Cs_8In_{27}Sb_{19}$, and other unconventional clathrates.[5,9,12] This model shows reasonable agreement with the HAADF-STEM images (Fig. 5). The $P2$ clathrate-I superstructure of $Cs_8Zn_{18}Sb_{28}$ has an 18 times larger volume and to the best of our knowledge would be the largest reported superstructure for any clathrate. With 972 atoms in the unit cell and a primitive unit cell volume of 28 828 Å^3, the crystal structure of $Cs_8Zn_{18}Sb_{28}$ approaches the complexity of giant unit cell intermetallics, such as $NaCd_2$, $R_{117}Co_{52}Sn_{112}$, and Eu_4Cd_{25}.[26–28] Possible explanations for this complex ordering could come from framework bond distance ordering (*i.e.* Zn–Sb bonds being shorter than Sb–Sb distances), an ordering of Cs vacancies, or a combination of both. To check for possible Cs vacancies, the synchrotron single crystal X-ray diffraction datasets were solved using a $Pm\bar{3}n$ subcell with a = 11.70 Å. The resulting composition was $Cs_{7.6(1)}Zn_{18}Sb_{28}$. EDX microprobe analysis resulted in lower vacancy concentration of $Cs_{7.8(1)}Zn_{17.5(1)}Sb_{28}$, normalizing to 28 Sb atoms (Table S6 and Fig. S2†).

We hypothesize that in the case of the $Cs_8Cd_{18}Sb_{28}$ clathrate, small displacements of Cs atoms from the center of cages created additional perturbation in Cd–Sb framework, which causes partial ordering and formation of a mixed occupied Cd/Sb site. In the case of $Cs_8Zn_{18}Sb_{28}$, the Zn/Sb cages are significantly smaller in size and a substantial fraction (~20%) of small pentagonal dodecahedral cages are empty resulting in overall $Cs_{7.6}Zn_{18}Sb_{28}$ composition. Similar levels of Cs vacancies were observed in the $Cs_8Zn_{18}As_{28}$ clathrate.[6] This ordering of guest vacancies may lead to the lowering of symmetry, as in the case of Si–P–Te clathrate-I.[29,30] In the case of $Cs_8Zn_{18}Sb_{28}$, the combination of the two possible driving forces, Zn/Sb ordering in the framework and Cs/vacancy ordering in the guest sublattice, resulted in the complex crystal structure with huge unit cell.

Ordered clathrate superstructures might not be stable at high temperatures. For example, A_8Sn_{44} (A = Cs, Rb, K) clathrates were shown to crystallize in $Ia\bar{3}d$ superstructure due to framework vacancies ordering. Upon heating, this superstructure collapses into a primitive disordered $Pm\bar{3}n$ type-I clathrate substructure.[31] We hypothesized that similar process may occur for $Cs_8M_{18}Sb_{28}$ clathrates. In the original report by Chen *et al.* the single crystals were selected from products of a reaction performed in CsCl flux at high temperatures, 1123 K.[18] This would explain why only disordered $Pm\bar{3}n$ type-I clathrate substructure was detected in the original report.

Mixed-metal clathrates, with both Zn and Cd in the framework, show a complete collapse of any superstructural ordering. For instance, the $Cs_8Zn_9Cd_9Sb_{28}$ clathrate has a unit cell length of 11.9595(7) Å and crystallizes in the archetypical type-I clathrate $Pm\bar{3}n$ (no. 223, Z = 1; Tables S1, S4 and S5†). This unit cell length is halfway between the normalized unit cell parameters for $Cs_8Zn_{18}Sb_{28}$ (11.70 Å) and $Cs_8Cd_{18}Sb_{28}$ (12.19 Å). No additional superstructural diffraction spots are found in the SC-XRD experiments and a structure solution can be achieved by allowing a mixing of Zn, Cd, and Sb on the three framework positions. Further information about this refinement can be

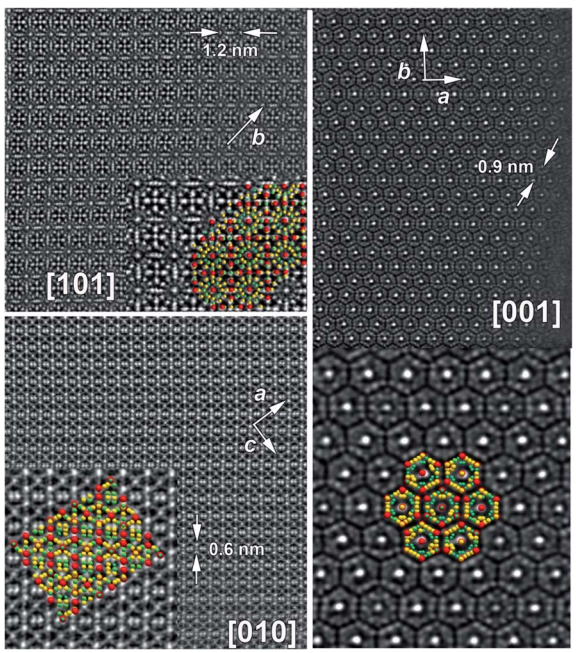

Fig. 5 HAADF-STEM images for select $Cs_8Zn_{18}Sb_{28}$ zone axis: [001] (right), [101] (top left), and [010] (bottom left). Magnified images and overlaid structural models in $P2$ superstructure model are given as insets, where (Cs – red; Zn – green; and Sb – yellow).

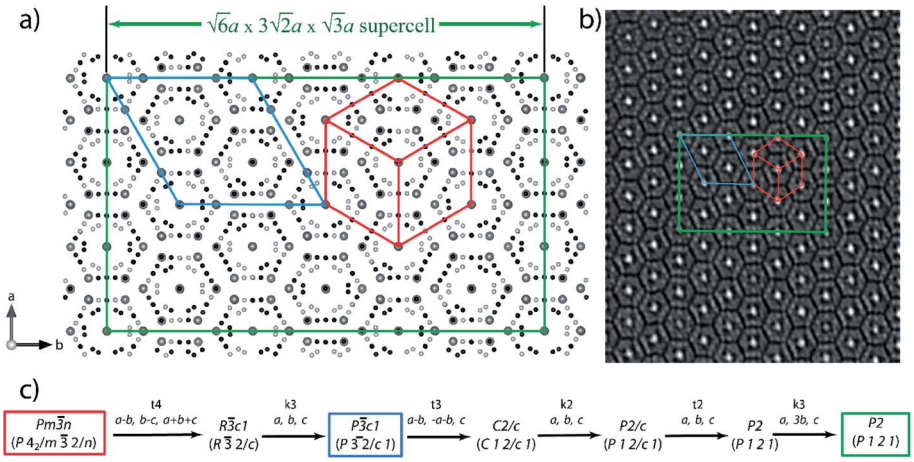

Fig. 6 (a) Projection of the $Cs_8Zn_{18}Sb_{28}$ clathrate superstructure, with the *Pm*$\bar{3}$*n* subcell (red), the *P*$\bar{3}$*c*1 supercell (blue), and *P*2 supercell (green) emphasized. Note the projection of the subcell is along the $[111]_C$ direction. (b) [001] HAADF-STEM image of $Cs_8Zn_{18}Sb_{28}$ with model unit cells drawn over: *P*2 (green), *P*$\bar{3}$*c*1 (blue), and *Pm*$\bar{3}$*n* (red). (c) Diagram showing the group–subgroup relationship between the ideal type-I clathrate *Pm*$\bar{3}$*n* subcell and the *P*2 supercell.

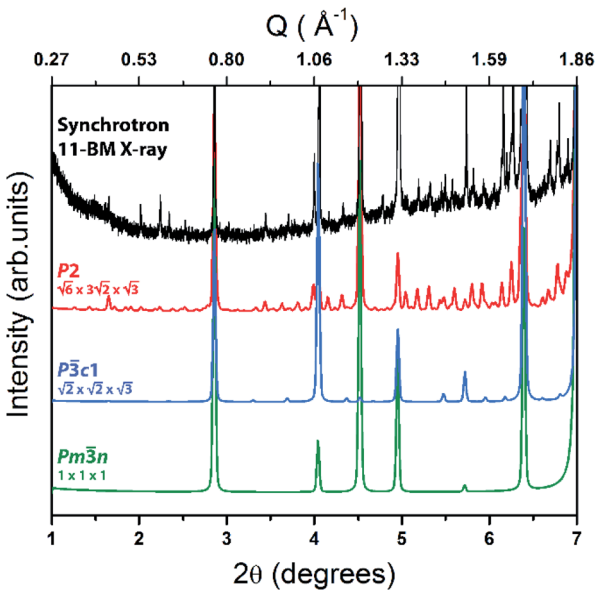

Fig. 7 High-resolution synchrotron PXRD pattern of $Cs_8Zn_{18}Sb_{28}$ (black) with the *P*2 (red), *P*$\bar{3}$*c*1 (blue), and *Pm*$\bar{3}$*n* (green) clathrate-I calculated patterns shown below.

found in the ESI.† Similar results are found for all SC-XRD experiments involving $Cs_8Zn_{18-x}Cd_xSb_{28}$ quaternary solid-solution compositions. These results are further corroborated by high-resolution synchrotron PXRD of $Cs_8Zn_9Cd_9Sb_{28}$, in which no superstructural peaks can be observed.

Synthesis and calorimetry

The synthesis of $Cs_8Zn_{18-x}Cd_xSb_{28}$ ($x = 0, 4.5, 9, 13.5, 18$) can be readily achieved through solid-state reaction of the elements. As Cs is highly volatile and reactive at high temperatures, the reaction must be carried out in sealed Ta ampoules to contain the alkali metal vapors. Samples run in open Ta crucibles resulted in complete removal of Cs from the sample due to reaction with the outer silica jacket. As Ta is prone to reaction with Sb at higher temperatures, annealing temperatures must be kept below 823 K to prevent the formation of Ta_3Sb. Homogenization and bulk sample stoichiometries was checked using SEM-EDX microprobe analysis (Table S6 and Fig. S2–S4†). Averaged EDX analysis confirms target compositions of $Cs_8Zn_{18-x}Cd_xSb_{28}$ ($x = 0$, 4.5, 9, 13.5, 18). The full series of dark gray products are air- and water-stable for extended periods of time, according to PXRD. SEM results indicate that exposure to ambient conditions can cause surface decomposition, though this seems to affect the surface only and not the bulk. The bulk stability is lost in acidic media, with the samples completely decomposing in 1 M HCl.

An alternative synthesis is presented in the 2009 work by Liu *et al.*, in which a CsCl flux is utilized and elemental Cs is not used.[18] In this synthesis, elemental Lu is added to the sample and acts as a sacrificial reactant to generate Cs *in situ*, resulting in formation of $Cs_8Zn_{18}Sb_{28}$ and $LuCl_3$. As the clathrate phase is water stable, water-soluble CsCl and $LuCl_3$ can be washed away. We have modified this synthesis to use Mg as the sacrificial reagent instead of expensive Lu, forming water-soluble $MgCl_2$ as the byproduct. The Mg-based synthesis boasts many advantages, such as: earth abundance, complete air-stability of all starting reagents, and easy scalability. This synthetic method may be useful for the safe production of other Cs-based compounds.[32,33] Unfortunately, this pathway always included small amounts of side products (~5–10 mol%), commonly elemental Sb or ZnSb.

Thermal stability of the clathrate series was studied using differential scanning calorimetry (Fig. S5†). A linear trend for the melting points is observed for all compounds (Fig. 8). $Cs_8Zn_{18}Sb_{28}$, $Cs_8Zn_{13.5}Cd_{4.5}Sb_{28}$, and $Cs_8Zn_9Cd_9Sb_{28}$ melt congruently at 963 K, 945 K, and 928 K, respectively. Cd-rich $Cs_8Zn_{4.5}Cd_{13.5}Sb_{28}$ and $Cs_8Cd_{18}Sb_{28}$ melt at 914 K and 901 K, respectively, but crystallize incongruently, showing multiple

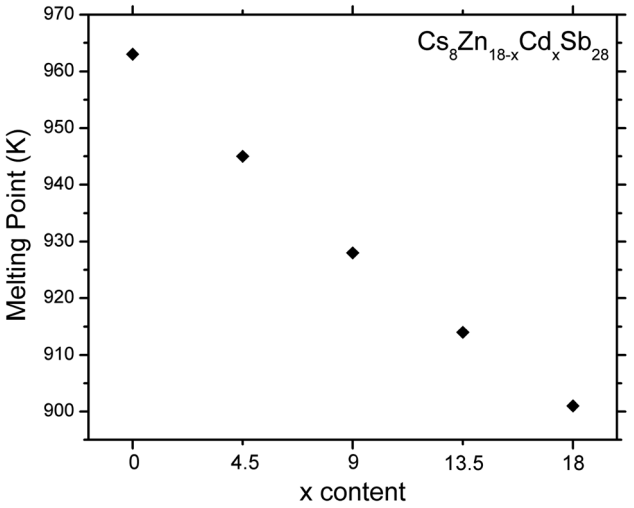

Fig. 8 Melting points for $Cs_8Zn_{18-x}Cd_xSb_{28}$ (x = 0, 4.5, 9, 13.5, 18). Estimated standard deviations are smaller than symbols used.

peaks upon cooling. PXRD indicates the secondary phase for $Cs_8Cd_{18}Sb_{28}$ as $Cs_2Cd_5Sb_4$ and for $Cs_8Zn_{4.5}Cd_{13.5}Sb_{28}$ to be a substituted modification of $Cs_2Cd_5Sb_4$ and $Cs_{16}Cd_{25}Sb_{36}$.[34] Interestingly, the reported melting point for $Cs_8Zn_{18}Sb_{28}$ is 900 K,[18] while we consistently produced a melting point of 963 K, measuring multiple samples from different synthesis. It is possible that clathrate samples with full ordering in the framework show higher thermal stability as compared to potentially disordered clathrates reported in the previous investigation.[18]

The formation and decomposition of $Cs_8Zn_{18}Sb_{28}$ was studied using variable temperature *in situ* synchrotron PXRD. As neither Cs nor Zn was easily fit into the small capillaries required for the experiment, a stoichiometric mixture of pre-synthesized CsSb, $CsSb_2$, Zn_8Sb_7, and Sb were used instead. A waterfall plots showing the progression of the reaction is shown in Fig. 9. As the capillary is heated, PXRD peaks that can be attributed to the $Cs_8Zn_{18}Sb_{28}$ phase begin to appear around 703 K. The full conversion to the clathrate phase is finished at 808 K, well in-line with the chosen synthetic temperature used (823 K). Increase of temperature to 952 K showed the melting of the clathrate phase, agreeing well with the observed DSC data. Additionally, a pre-synthesized $Cs_8Zn_{18}Sb_{28}$ sample was studied, also exhibiting a similar melting point of 955 K (data not shown).

Transport properties

Thermal and charge transport properties were investigated for the $Cs_8Zn_{18-x}Cd_xSb_{28}$ (x = 0, 4.5, 9, 13.5, 18) on highly dense sintered pellets. All measured compounds show remarkably low thermal conductivities, with values below 1 W m^{-1} K^{-1} at 300 K (Fig. 10a). $Cs_8Zn_{18}Sb_{28}$ and $Cs_8Cd_{18}Sb_{28}$ show the highest values at room temperature; 0.79 and 0.65 W m^{-1} K^{-1}, respectively. The mixed metal framework clathrates, $Cs_8Zn_{13.5}Cd_{4.5}Sb_{28}$, $Cs_8Zn_9Cd_9Sb_{28}$, and $Cs_8Zn_{4.5}Cd_{13.5}Sb_{28}$, have additional sources of phonon scattering from disorder associated with Zn/Cd distribution within their framework and have significantly lower room temperature thermal conductivities of 0.55, 0.49, and 0.49 W m^{-1} K^{-1}, respectively. While low thermal conductivity is expected for clathrates, most falling below 3 W m^{-1} K^{-1} at room temperature,[1,2] values of ~0.5 W m^{-1} K^{-1} are only observed by the tin tetrel clathrates.[1] For instance, several compositions close to $Ba_8Ga_{16}Sn_{30}$ have total thermal conductivities close to 0.7 W m^{-1} K^{-1} at 300 K.[35–37] These thermal conductivities are similar to the tetrel-free clathrate $Ba_8Au_{16}P_{30}$, which has a room temperature thermal conductivity of 0.6 W m^{-1} K^{-1}.[9] To the best of our knowledge, the thermal conductivities of $Cs_8Zn_9Cd_9Sb_{28}$ and $Cs_8Zn_{4.5}Cd_{13.5}Sb_{28}$ are among the lowest reported for any clathrate composition for reasonably dense measured samples, *i.e.* >80% compared to X-ray density. The total thermal conductivities of $Cs_8Zn_{18-x}Cd_xSb_{28}$ clathrates are also lower than those (0.65–1 W m^{-1} K^{-1}) for complex binary Zn–Sb and Cd–Sb phase with significant degree of disorder and structural complexity.[14,38–40]

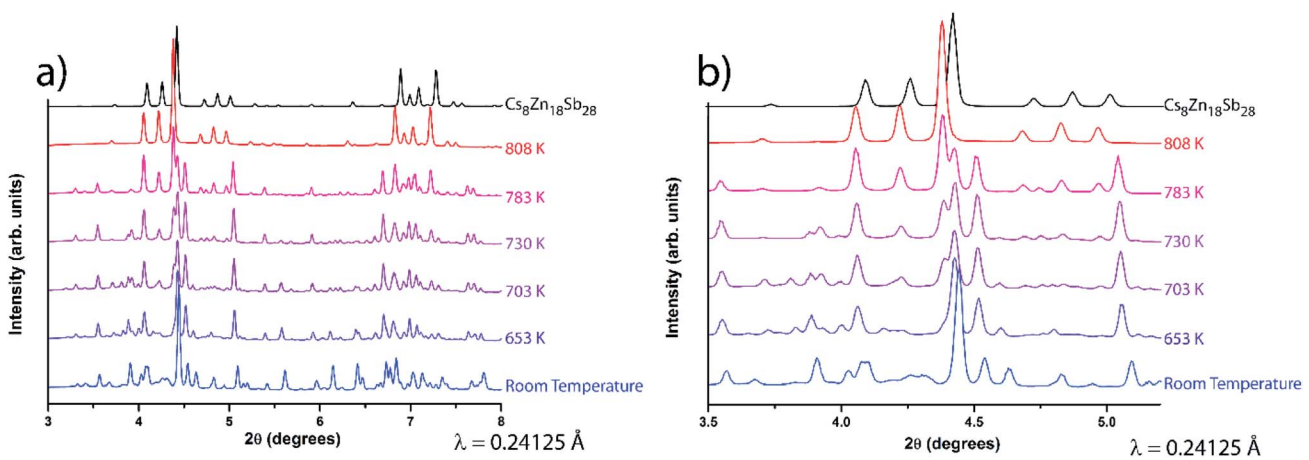

Fig. 9 *In situ* variable temperature synchrotron PXRD of sample consisting of CsSb, $CsSb_2$, Zn_8Sb_7, and Sb mixture in a combined ratio of $Cs_8Zn_{18}Sb_{28}$; (a) full patterns and (b) selected 2θ range. The sample was heated from room temperature (bottom pattern) to 808 K (second to top pattern). A calculated pattern for $Cs_8Zn_{18}Sb_{28}$ at room temperature is shown for comparison (top black pattern).

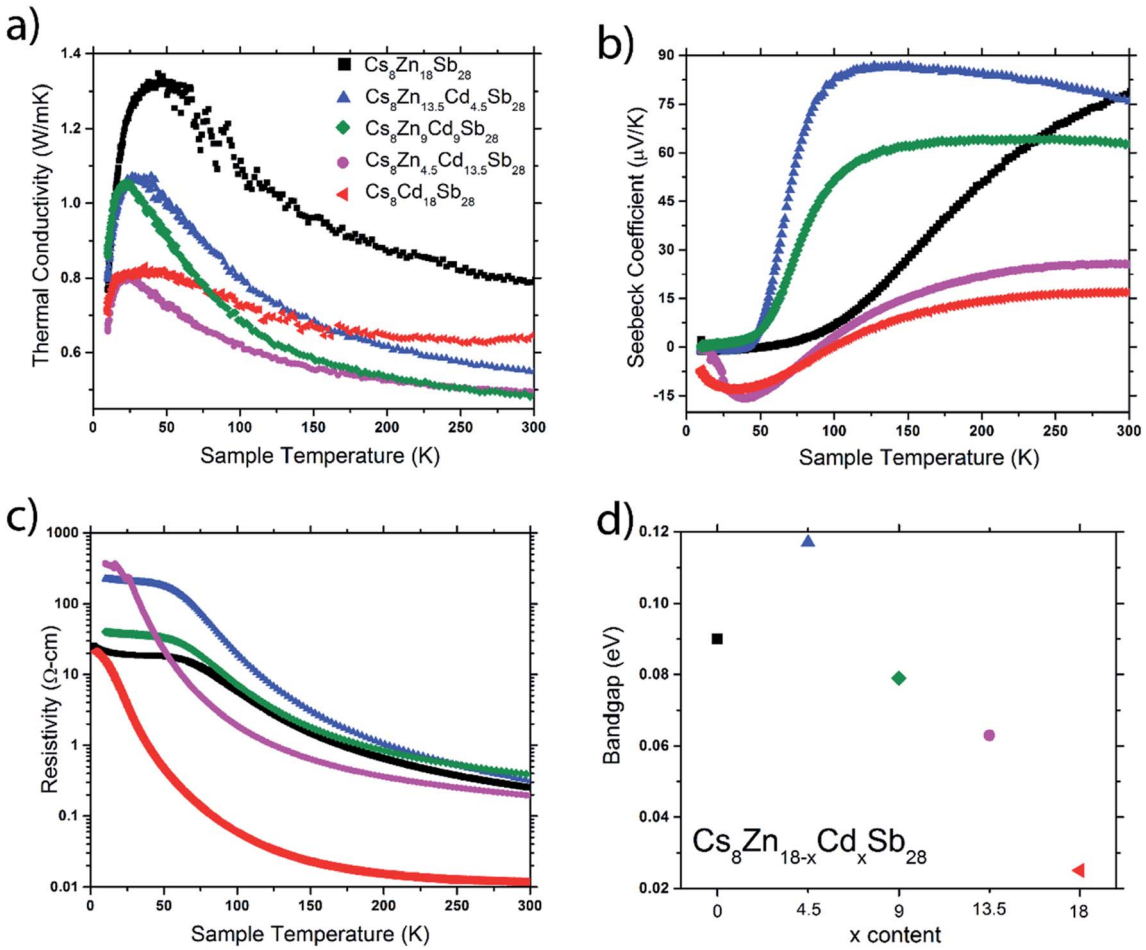

Fig. 10 Thermal and charge transport properties of $Cs_8Zn_{18-x}Cd_xSb_{28}$ (x = 0, 4.5, 9, 13.5, 18): (a) thermal conductivity, (b) Seebeck coefficient, and (c) electrical resistivity. Additionally, estimated bandgaps using high-temperature part of the electrical resistivity data is shown in (d).

$Cs_8Zn_{18}Sb_{28}$ shows a regular Seebeck coefficient temperature dependence for a p-type semiconducting material, reaching a value of 80 μV K^{-1} at 300 K (Fig. 10b). The thermopower behavior for the other clathrate samples is not as straightforward. $Cs_8Cd_{18}Sb_{28}$ and the Cd-rich $Cs_8Zn_{4.5}Cd_{13.5}Sb_{28}$ clathrates show a n–p transition at low temperatures, changing slopes around 35 K and finally moving into the p-type regime near 100 K resulting in moderate values of 17 and 26 μV K^{-1} at 300 K, respectively. This charge carrier change can be explained by low-laying impurity states in the band structure, allowing for n-type conducting until the temperature was sufficient to thermally activate holes over the bandgap. For the Zn-rich quaternary clathrates, $Cs_8Zn_{13.5}Cd_{4.5}Sb_{28}$ and $Cs_8Zn_9Cd_9Sb_{28}$, a strikingly quick increase of the Seebeck is observed at 50 to 75 K. After this rapid increase, a Seebeck plateau is held until values of 76 and 63 μV K^{-1} are reached at 300 K, respectively. For $Cs_8Zn_{13.5}Cd_{4.5}Sb_{28}$, a maximum Seebeck for all measured clathrates of 87 μV K^{-1} is found before the plateau at 145 K.

All clathrate samples show an exponential temperature dependence in electrical resistivity (Fig. 10c) in the 100–300 K range, with room temperature values of 250, 310, 380, 190, and 1.2 mΩ cm for $Cs_8Zn_{18-x}Cd_xSb_{28}$ (x = 0, 4.5, 9, 13.5, 18) respectively. As the samples move from Zn to Cd compositions, an initial increase in the room temperature electrical resistivity is observed and may be correlated to the reduction of the superstructural ordering, creating a disordered framework that allows for additional scattering of the charge carriers. As Cd becomes more prevalent within the framework, the electrical resistivity begins to drop and eventually leads to a significant reduction for the Zn-free composition. For the Zn-rich compositions, $Cs_8Zn_{18}Sb_{28}$, $Cs_8Zn_{13.5}Cd_{4.5}Sb_{28}$ and $Cs_8Zn_9Cd_9Sb_{28}$, a noticeable slope change in the resistivity is present between 50 K and 75 K and aligns well with features observed in the Seebeck curves. This slope change is easier seen by plotting $\ln(\rho^{-1})$ *vs.* T^{-1} (Fig. S6†). Fitting the two slopes gives transition temperatures of 80 K, 71 K, and 70 K for $Cs_8Zn_{18}Sb_{28}$, $Cs_8Zn_{13.5}Cd_{4.5}Sb_{28}$ and $Cs_8Zn_9Cd_9Sb_{28}$, respectively.

Additionally, bandgaps can be extracted by fitting the resistivity to $\ln(1/\rho) = -E_a/2k_BT$, where k_B is a Boltzmann constant (Fig. 10d). A nonlinear trend is found in the calculated bandgap between the two parent compositions with calculated bandgaps of 0.09 and 0.025 eV for $Cs_8Zn_{18}Sb_{28}$ and $Cs_8Cd_{18}Sb_{28}$, respectively (Fig. 10d). This nonlinear trend in solid-solutions is not unheard of and can be found in many systems, such as:

$K_2Bi_{8-x}Sb_xSe_{13}$, $CH_3NH_3Sn_{1-x}Pb_xI_3$, and $Pb_{1-x}Sn_xTe$.[41–43] Explanations to the anomalous behavior is often attributed to inhomogeneous distribution of the substituted element and formation of impurity states within the band structure.

Conclusion

Reinvestigation of $Cs_8Zn_{18}Sb_{28}$ and $Cs_8Cd_{18}Sb_{28}$ was performed, both of which exhibit unique and complex crystallographic superstructures not initially reported. SC-XRD shows that $Cs_8Cd_{18}Sb_{28}$ adopts a body centered cubic superstructure, space group $Ia\bar{3}d$ (no. 230), doubling the unit cell length to 24.3160(5) Å and 8-fold volume increase. Cd and Sb segregates into individual positions, reducing the number of Cd–Cd interactions present within the framework. This complex model features one framework position that has split into three individual sites, one of which appears to be coupled with a Cs vacancy within the small cage. Additionally, the Cs guest position residing in the large cage splits into a secondary site, a phenomenon not uncommon in low temperature clathrate crystal structures. The structure of $Cs_8Zn_{18}Sb_{28}$ has proven to be more complex and not easily solved through SC-XRD experiments due to extensive twinning. HAADF-STEM and ED of $Cs_8Zn_{18}Sb_{28}$ was used to help explore this structural ordering. Diffraction data clearly shows the unit cell expansion and reduction of symmetry for the structure. Examination of this data with the HAADF-STEM images suggests that $Cs_8Zn_{18}Sb_{28}$ orders in a monoclinic cell that is $\sqrt{6}\times3\sqrt{2}\times\sqrt{3}$ compared to the primitive unit cell.

A full solid solution between the Zn- and Cd-parent compounds is synthetically accessible, with stoichiometries and homogeneity confirmed through SEM EDX microprobe mapping. These mixed-metal clathrates show a collapse of any superstructural ordering crystallizing in the clathrate-I archetype structure in $Pm\bar{3}n$ space group. Primitive unit cell sizes and thermal melting points follow Vegard's law, with linear trends between the two parent materials. Variable temperature *in situ* synchrotron powder X-ray diffraction of $Cs_8Zn_{18}Sb_{28}$ corroborates the DSC melting point and indicates that the clathrate begins forming well below the chosen synthesis temperature of 823 K.

Thermal conductivities for the clathrates are surprisingly low, all falling below 0.8 W m^{-1} K^{-1} at room temperature and a remarkably low value of 0.49 W m^{-1} K^{-1} for $Cs_8Zn_9Cd_9Sb_{28}$ and $Cs_8Zn_{4.5}Cd_{13.5}Sb_{28}$ clathrates. $Cs_8Zn_{18}Sb_{28}$ has typical p-type semiconductor charge transport properties, while the remaining clathrates show unusual n–p transitions or steep increases of Seebeck values at low temperatures. Extraction of the bandgaps for the series show an anomalous widening and then shrinking of the bandgap with increasing Cd-content.

Funding

This research was supported by the U.S. Department of Energy, Office of Basic Energy Sciences, Division of Materials Science and Engineering under Award DE-SC0008931. PY was supported by the Chateaubriand Fellowship of the Office for Science & Technology of the Embassy of France in the United States. NSF's ChemMatCARS Sector 15 is supported by the Divisions of Chemistry (CHE) and Materials Research (DMR), National Science Foundation, under grant number NSF/CHE-1834750. Use of the Advanced Photon Source, an Office of Science User Facility operated for the U.S. Department of Energy (DOE) Office of Science by Argonne National Laboratory, was supported by the U.S. DOE under Contract No. DE-AC02-06CH11357. This research used resources of the Advanced Light Source, which is a DOE Office of Science User Facility under contract no. DE-AC02-05CH11231.

Author contributions

The manuscript was written through contributions of all authors.

Conflicts of interest

Authors declare no conflict of interests.

Acknowledgements

The authors are thankful to Dr S. Lapidus, Dr W. Xu, and Dr A. Yakovenko (APS ANL) for help with collecting high-resolution and *in situ* synchrotron XRD patterns, and Prof. J. Zaikina (ISU) for access to the SPS and arc-welder.

References

1 J.-A. Dolyniuk, B. Owens-Baird, J. Wang, J. V. Zaikina and K. Kovnir, *Mater. Sci. Eng., R*, 2016, **108**, 1–46.
2 *The Physics and Chemistry of Inorganic Clathrates*, ed. G. S. Nolas, Springer, Dordrecht, 2014.
3 M. Christensen, N. Lock, J. Overgaard and B. B. Iversen, *J. Am. Chem. Soc.*, 2006, **128**(49), 15657–15665.
4 J.-A. Dolyniuk, J. Wang, K. Lee and K. Kovnir, *Chem. Mater.*, 2015, **27**(12), 4476–4484.
5 J. Dünner and A. Mewis, *Z. Anorg. Allg. Chem.*, 1995, **621**(2), 191–196.
6 H. He, A. Zevalkink, Z. M. Gibbs, G. J. Snyder and S. Bobev, *Chem. Mater.*, 2012, **24**(18), 3596–3603.
7 I. V. Plokhikh, N. Khan, A. A. Tsirlin, A. N. Kuznetsov, D. O. Charkin, A. V. Shevelkov and A. Pfitzner, *Inorg. Chem. Front.*, 2020, **7**(5), 1115–1126.
8 J. Wang, J.-A. Dolyniuk and K. Kovnir, *Acc. Chem. Res.*, 2018, **51**(1), 31–39.
9 J. Fulmer, O. I. Lebedev, V. V. Roddatis, D. C. Kaseman, S. Sen, J.-A. Dolyniuk, K. Lee, A. V. Olenev and K. Kovnir, *J. Am. Chem. Soc.*, 2013, **135**(33), 12313–12323.
10 J. Dolyniuk, P. S. Whitfield, K. Lee, O. I. Lebedev and K. Kovnir, *Chem. Sci.*, 2017, **8**(5), 3650–3659.
11 J. Wang, O. I. Lebedev, K. Lee, J.-A. Dolyniuk, P. Klavins, S. Bux and K. Kovnir, *Chem. Sci.*, 2017, **8**(12), 8030–8038.
12 B. Owens-Baird, J. Wang, S. G. Wang, Y.-S. Chen, S. Lee, D. Donadio and K. Kovnir, *J. Am. Chem. Soc.*, 2020, **142**(4), 2031–2041.

13 J. Lin, X. Li, G. Qiao, Z. Wang, J. Carrete, Y. Ren, L. Ma, Y. Fei, B. Yang, L. Lei and J. Li, *J. Am. Chem. Soc.*, 2014, **136**(4), 1497–1504.
14 J. Wang and K. Kovnir, *J. Am. Chem. Soc.*, 2015, **137**(39), 12474–12477.
15 G. J. Snyder, M. Christensen, E. Nishibori, T. Caillat and B. B. Iversen, *Nat. Mater.*, 2004, **3**, 458.
16 Y. Mozharivskyj, Y. Janssen, J. L. Harringa, A. Kracher, A. O. Tsokol and G. J. Miller, *Chem. Mater.*, 2006, **18**(3), 822–831.
17 J. Nylén, M. Andersson, S. Lidin and U. Häussermann, *J. Am. Chem. Soc.*, 2004, **126**(50), 16306–16307.
18 Y. Liu, L.-M. Wu, L.-H. Li, S.-W. Du, J. D. Corbett and L. Chen, *Angew. Chem.*, 2009, **121**(29), 5409–5412.
19 L.-H. Li, L. Chen, J.-Q. Li and L.-M. Wu, *Chem. Mater.*, 2010, **22**(13), 4007–4018.
20 K. E. Woo, J. Wang, K. Wu, K. Lee, J.-A. Dolyniuk, S. Pan and K. Kovnir, *Adv. Funct. Mater.*, 2018, **28**(30), 1801589.
21 B. C. Chakoumakos, B. C. Sales and D. G. Mandrus, *J. Alloys Compd.*, 2001, **322**(1), 127–134.
22 B. C. Chakoumakos, B. C. Sales, D. G. Mandrus and G. S. Nolas, *J. Alloys Compd.*, 2000, **296**(1), 80–86.
23 N. L. Okamoto, J.-H. Kim, K. Tanaka and H. Inui, *Acta Mater.*, 2006, **54**(20), 5519–5528.
24 B. C. Sales, B. C. Chakoumakos, R. Jin, J. R. Thompson and D. Mandrus, *Phys. Rev. B: Condens. Matter Mater. Phys.*, 2001, **63**(24), 245113.
25 J.-A. Dolyniuk, J. Wang, M. A. T. Marple, S. Sen, Y. Cheng, A. J. Ramirez-Cuesta and K. Kovnir, *Chem. Mater.*, 2018, **30**(10), 3419–3428.
26 C. Pay Gómez and S. Lidin, *Chem.–Eur. J.*, 2004, **10**(13), 3279–3285.
27 K. Kovnir and M. Shatruk, *Eur. J. Inorg. Chem.*, 2011, (26), 3955–3962.
28 S. Samson, *Nature*, 1962, **195**(4838), 259–262.
29 J. V. Zaikina, K. A. Kovnir, U. Burkhardt, W. Schnelle, F. Haarmann, U. Schwarz, Y. Grin and A. V. Shevelkov, *Inorg. Chem.*, 2009, **48**(8), 3720–3730.
30 J. V. Zaikina, K. A. Kovnir, U. Schwarz, H. Borrmann and A. V. Shevelkov, *Z. Kristallogr. - New Cryst. Struct.*, 2007, **222**(3), 177.
31 A. Kaltzoglou, T. Fässler, M. Christensen, S. Johnsen, B. Iversen, I. Presniakov, A. Sobolev and A. Shevelkov, *J. Mater. Chem.*, 2008, **18**(46), 5630–5637.
32 K. E. Woo, J.-A. Dolyniuk and K. Kovnir, *Inorg. Chem.*, 2019, **58**(8), 4997–5005.
33 P. Yox, J. Wang and K. Kovnir, *Front. Chem.*, 2020, **8**, 186.
34 B. Owens-Baird, *Structure-property relationships of binary and ternary metal pnictides for energy applications*, Iowa State University, 2019.
35 B. Du, Y. Saiga, K. Kajisa and T. Takabatake, *J. Appl. Phys.*, 2012, **111**(1), 013707.
36 Y. Saiga, K. Suekuni, S. K. Deng, T. Yamamoto, Y. Kono, N. Ohya and T. Takabatake, *J. Alloys Compd.*, 2010, **507**(1), 1–5.
37 K. Suekuni, M. A. Avila, K. Umeo, H. Fukuoka, S. Yamanaka, T. Nakagawa and T. Takabatake, *Phys. Rev. B: Condens. Matter Mater. Phys.*, 2008, **77**(23), 235119.
38 T. Caillat, J. P. Fleurial and A. Borshchevsky, *J. Phys. Chem. Solids*, 1997, **58**(7), 1119–1125.
39 S. Wang, J. Yang, L. Wu, P. Wei, J. Yang, W. Zhang and Y. Grin, *Chem. Mater.*, 2015, **27**(3), 1071–1081.
40 B. Zhou, C. Sun, X. Wang, Z. Bu, W. Li, R. Ang and Y. Pei, *ACS Appl. Mater. Interfaces*, 2019, **11**(30), 27098–27103.
41 I. U. Arachchige and M. G. Kanatzidis, *Nano Lett.*, 2009, **9**(4), 1583–1587.
42 F. Hao, C. C. Stoumpos, R. P. H. Chang and M. G. Kanatzidis, *J. Am. Chem. Soc.*, 2014, **136**(22), 8094–8099.
43 T. Kyratsi, J. S. Dyck, W. Chen, D.-Y. Chung, C. Uher, K. M. Paraskevopoulos and M. G. Kanatzidis, *J. Appl. Phys.*, 2002, **92**(2), 965–975.

